PAPER

Nano-fabrication of depth-varying amorphous silicon crescent shell array for light trapping

To cite this article: Huan Yang *et al* 2017 *Nanotechnology* **28** 505301

View the article online for updates and enhancements.

Nano-fabrication of depth-varying amorphous silicon crescent shell array for light trapping

Huan Yang[1] , Ben Q Li[1,2], Xinbing Jiang[1], Wei Yu[1] and Hongzhong Liu[1]

[1] Micro- and Nano-manufacturing Research Center, State Key Laboratory for Manufacturing Systems Engineering, Xi'an Jiaotong University, 28 Xianning Road, Xi'an 710049, People's Republic of China
[2] Department of Mechanical Engineering, University of Michigan-Dearborn, Dearborn, MI 48128, United States of America

E-mail: benqli@umich.edu

CrossMark

Abstract

We report a new structure of depth controllable amorphous silicon (a-Si) crescent shells array, fabricated by the SiO_2 monolayer array assisted deposition of a-Si by plasma enhanced chemical vapor deposition and nanosphere lithography, for high-efficiency light trapping applications. The depth of the crescent shell cavity was tailored by selective etching of a-Si layer of the SiO_2/a-Si core/shell nanoparticle array with a varied etching time. The morphological changes of the crescent shells were examined by scanning electron microscopy and atomic force microscopy. A simple model is developed to describe the geometrical evolution of the a-Si crescent shells. Spectroscopic measurements and finite difference time domain simulations were conducted to examine the optical performance of the crescent shells. Results show that these nanostructures all have a broadband high efficiency absorption and that the light trapping capability of these crescent shell structures depends on the excitation of depths-regulated optical resonance modes. With an appropriate selection of process parameters, the structure of crescent a-Si shells may be fine-tuned to achieve an optimal light trapping capacity.

Keywords: crescent shell, nanosphere lithography, depth-controllable, light trapping, resonance mode

(Some figures may appear in colour only in the online journal)

Introduction

Efficient light management is crucial for improving the performance of optoelectronic devices such photodetectors and solar cells. Studies show that nanostructured photonic materials, designed to enhance the effective optical path length, hold a great promise to harvest incoming photons with various light management schemes, such as antireflection or resonance absorption or both [1–5]. Semiconductor nanostructures, properly designed and fabricated, may simultaneously shorten the photon-generated carrier collection length and impede carrier recombination, resulting in more effective carrier collection for performance enhancement of photodetectors and solar cells. By far, a variety of nanostructures, including nanopyramids [6, 7], nanowire [8–10], nanopillars [11, 12], nanocone [13–15], nanohole [16–18], nanodome [19], nanoshell [20, 21], have been explored. In particular, nanoshells of applied light wavelength scale have been demonstrated with a promising capability of trapping sunlight within the shell structure over a broadband wavelength. A salient feature of the semiconductor nanoshells is that the energy entered into the shell nanostructure recirculates within the closed spherical shell by exciting the resonances at certain wavelengths, resulting in enormously enlarged optical path length in the active material [20, 22–24]. Furthermore, the resonance wavelengths can be regulated by the size of the shell cavity to enhance the light trapping capacity near the bandgap. Our finite difference time domain (FDTD)

1

simulations show that the light trapping capacity of the shell structures can be further enhanced by optimizing the design of nanostructure to improve optical resonance processes. One of these designs is the crescent nanoshell structure of varying depths, with which light trapping capability of the structure may be tuned to selectively excite optical resonance in broadband regime.

Many methods for fabricating of nanostructures have been developed, which include photolithography, electron beam lithography, x-ray lithography, dip-pen lithography, nanoimprinting, and soft lithography [25–29]. However, to fabricate such highly ordered shell arrays structure with feature sizes down to the wavelength scale, surface-patterning methods employing templates prepared by self-assembly of monolayer nanoparticles array are recognized to be a cost effective strategy [30–32]. The shell structures can be then fabricated via coating the surface of the spherical particles through wet or dry deposition methods. The wet methods involving solution reaction and electro- or electroless chemical deposition were applied for metal or solution synthesized compounds [33–37], while dry methods including physical and chemical deposition were widely employed to fabricate semiconductor structures [38–40]. Although varieties of shell structures have been reported, the investigation of fabrication of the crescent shell arrays structure with controlled depths has not been mentioned.

In this paper, we present a new nanosphere-based lithography method for fabricating two dimensional a-Si crescent shell array with controlled shell cavity depth. The process involves patterning with a monolayer of the SiO_2 array, followed by plasma enhanced chemical vapor deposition (PECVD) of a-Si shell and then by controlled reactive ion etching (RIE). We first describe the fabrication process and characterize the morphological changes of the etching process. Then, a model describing these etching time dependent shell depth is put forward and we demonstrate the fabrication of two dimensional a-Si shell array with controlled depth. The optical performance of these crescent structures is investigated by means of visible-NIR spectroscopy and FDTD simulations. It is shown that the structure of a-Si crescent shell can be applied to enhance the light absorption efficiency by realizing enhanced broadband whispering gallery mode (WGM) with an optimal crescent cavity depth.

Experimental section

Preparation of a monolayer of SiO_2/a-Si core/shell array

The SiO_2 colloidal particles were prepared by the Stöber method. The diameter of the particles was regulated by adjusting the volume ratio of the Tetraethyl orthosilicate (TEOS), ammonia and ethanol [41]. Typically, 8 ml ammonia was added to 25 ml ethanol and stirring kept for 30 min to make them uniformly mixed. 1 ml TEOS was then quickly added to the mixture, and the solution was stirred for 8 h to obtain SiO_2 colloids with diameter of ~320 nm. The prepared colloids were purified by repeated centrifugations (5 cycles),

and then re-dispersed in butyl alcohol with a concentration of 10% in weight. In order to prepare a monolayer of SiO_2 particles, 10 μl of the prepared colloids was dropped into water in a petri dish with a size of 6 cm. The SiO_2 particles were rapidly spreading out on the water/air interface and a closely arranged monolayer of SiO_2 particles array was formed in 1 min due to the immiscibility of water and butyl alcohol [42].

The fabrication process for the a-Si crescent shell arrays sample was briefly illustrated in figure 1. A monolayer of closely arranged silica particles was prepared on the substrate by gently immersing the substrate into the water and lifted up under a small angle. The substrate was a pre-cleaned glass slide coated with 200 nm Al layer by magnetic sputtering. The oxygen plasma clean was applied to make the substrate surface hydrophilic. A ~50 nm amorphous a-Si film was deposited around the SiO_2 particles on the substrate by PECVD, resulting in the SiO_2/a-Si core/shell particle array (see figure 1(a)). Because the reactive species are accelerated perpendicularly to the sample in a unidirectional electric field in the deposition chamber, the density of the accessible ionized gases decreased from the upper surface to the lower surface of the SiO_2/a-Si particles. Therefore, the thickness of the coated a-Si layer gradually decreases to zero along the direction from the top of the particle to the contact point between the particle and the substrate. As a result, the deposited a-Si layer was in the shape of inverted crescent shell. An epoxy resin layer (~2 mm) then was coated on the samples by letting a resin droplet undergo free spreading, followed by curing at 55 °C for an hour (see figure 1(b)). Then, the SiO_2/a-Si core/shell array was transferred to the epoxy resin layer by removing the Al layer in diluted hydrochloric acid (10% v/v). Inverting the epoxy layer exposes to air an array of up-right crescent a-Si shells coated on the SiO_2 particles (see figure 1(c)). The crescent a-Si shells was tailored by RIE, and the SiO_2 cores were then removed by immersing the sample in hydrofluoric acid (5% v/v) for 150 s, leaving as the final product of an array of crescent a-Si shell cavity with a controlled cavity depth (see figure 1(d)).

Etching process

The structure of well-prepared monolayer of SiO_2/a-Si particles array was tailored by the RIE (Oxford Plasmalab). The samples were put into a RIE chamber at a pressure of 10 mTorr. A flow of mixture gases of 60 standard cubic centimeters SF_6 and 30 standard cubic centimeters Ar per minute (SCCM) was used to generate reactive ions. A forward power and ICP power of 25 W and 450 W was applied, respectively.

Characterization

The morphological changes of the crescent shell for different RIE times were characterized by scanning electron microscopy (SEM) and atomic force microscopy (AFM). SEM observations were conducted on a Hitachi field emission electron microscope. AFM measurements were performed using a Bruker scanning probe microscope. The transmission
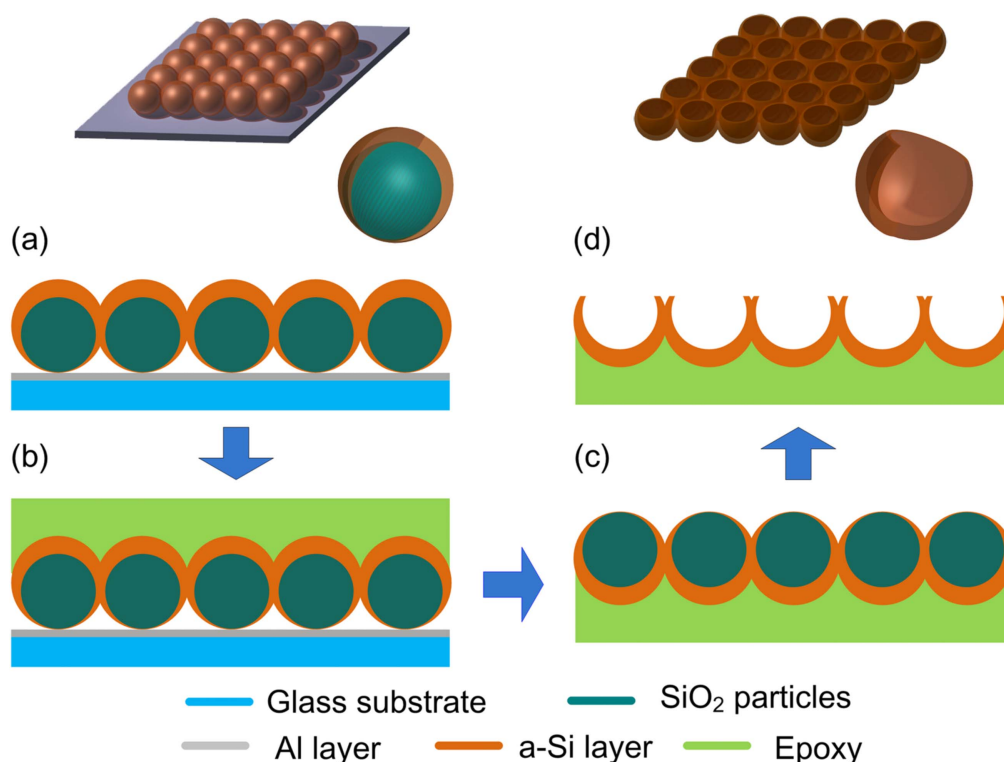
Figure 1. The schematic of fabrication of a-Si crescent shell.

and reflectance spectra of the samples were measured by UV–vis-NIR spectrometer with an integrating sphere (UV3600 Shimadzu).

Results and discussions

Figure 2 shows the various stages of the morphological changes of the crescent shells during etching. The SEM images in figure 2(A) show both the normal (upper row) and cross sectional view (lower row) of the a-Si crescent shell array with the etching times of $t = 0$, 3 s, 5 s, 7 s, and 13 s, which were marked by $0'$, $3'$, $5'$, $7'$ and $13'$ respectively. The corresponding AFM scans of 3, 5, 7 and 13 s are shown in figure 2(B).

The SEM image at $t = 0$, marked by $0'$, illustrates the morphology of the pristine sample of the SiO_2/a-Si core/shell arrays, which was just transferred from the substrate by etching out the sacrificial layer of Al. The view is on the side where the arrays were in contact with Al. A small dark point appearing at the top of every SiO_2/a-Si core/shell particle is a hole in the a-Si shell, which was created because the PECVD deposition of a-Si was not possible right at the contact point between the SiO_2 particle and the substrate. The SEM image right below is the cross sectional view of the arrays at $t = 0$. The SiO_2 core was etched for a better illustration of the shell structure. Clearly, the a-Si shell exhibits a crescent structure in that the a-Si layer is thinnest near the hole and gradually increases in thickness from the top to the bottom. To create a depth-dependent a-Si crescent structure, appropriate control

of a-Si etching time is required to ensure that the delicate crescent shell structure is maintained. Apparently, the time required depends on many process parameters, including the thickness of the a-Si layer, the SiO_2 particle size, and the final depth of the crescent structure.

With etching time set at $t = 3$ s, a layer of a-Si near the top of the crescent arrays was removed. This was followed by the removal of SiO_2 particle template, leaving an a-Si crescent shell with a defined depth. The result is shown in the SEM image marked by $3'$ in figure 2(A), right below which is the SEM image of the cross section of the structure. Apparently, the hole at the top was opened up to $d = \sim225$ nm at $t = 3$ s from a few nanometers at $t = 0$. The cross section of the a-Si cavity structure is characterized by a crescent spherical shell, which gradually increases in thickness from the top to the bottom. The depth of the shell cavity, measured from the bottom to the top opening, is ~282 nm.

With etching time increased to 5 s, the size of the hole was enlarged to ~252 nm and the depth of the cavity decreased. These results were further confirmed by the AFM measured results shown in figure 2(B). Particularly, the depth in 3 s etched shell looks smaller than the 5 s etched case in the AFM line scan profile showed in panel B. Noticing these sharp troughs in the line profiles of the 3 s etched shell, it can be concluded the opening mouth of the 3 s etched shell is so small that the AFM tip could not touch the lower surface inside the shell. Therefore, the depth shown in the scan curve is much smaller than the real size of the crescent shell. Finally, the opening diameters is ~318 nm after 13 s etching, which is close to the size of the inner SiO_2 particle. Besides, the rim of cavities was partially
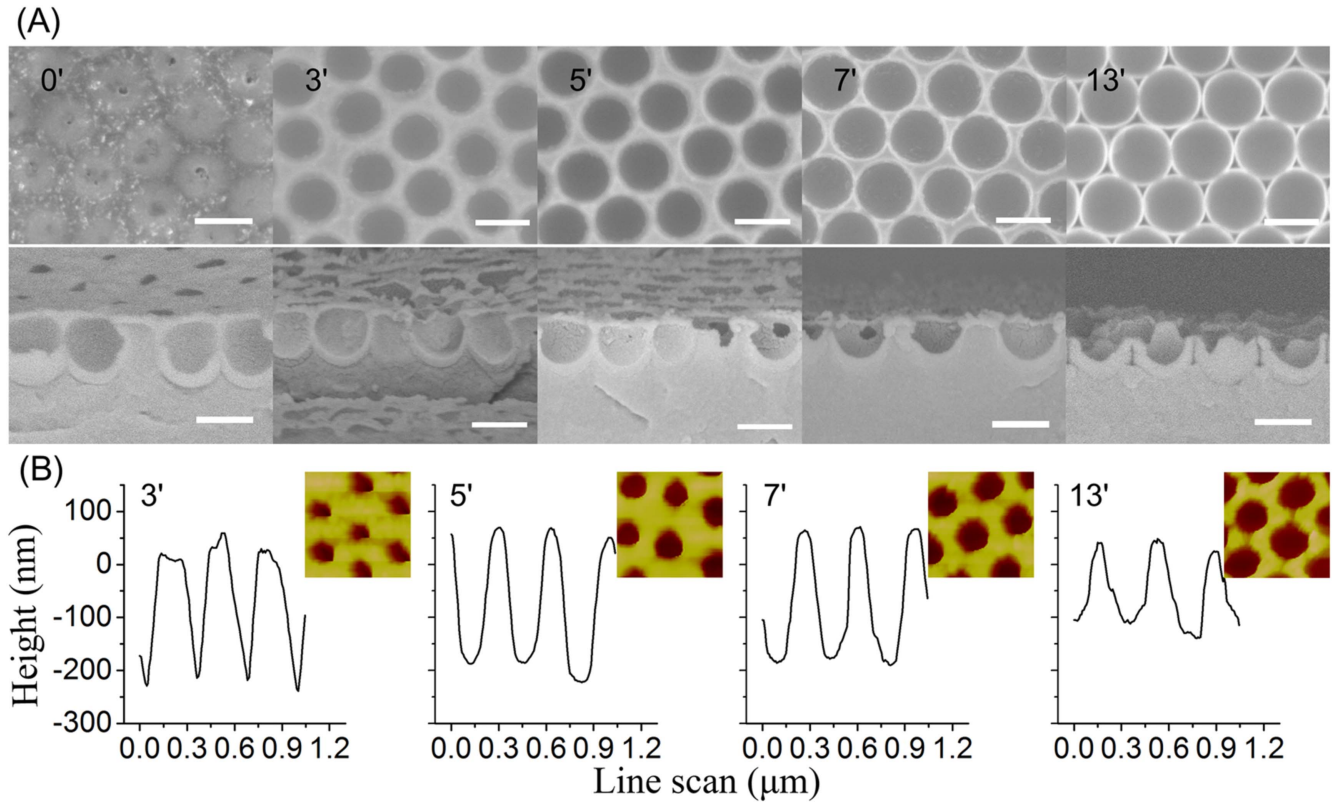
(A)

(B)

Figure 2. SEM images (panel A) and AFM scans (panel B) showing the morphological changes of the crescent a-Si shell cavity with an inner diameter $D = \sim320$ nm during the etching process. The SEM images are the normal and cross sectional views of the a-Si shell cavity array etched for 0 s, 3 s, 5 s, 7 s, and 13 s marked correspondingly by 0′, 3′, 5′, 7′ and 13′. Scale bars: 300 nm. The AFM line-scan profiles are taken through the center of the crescent shell shown in the insets.
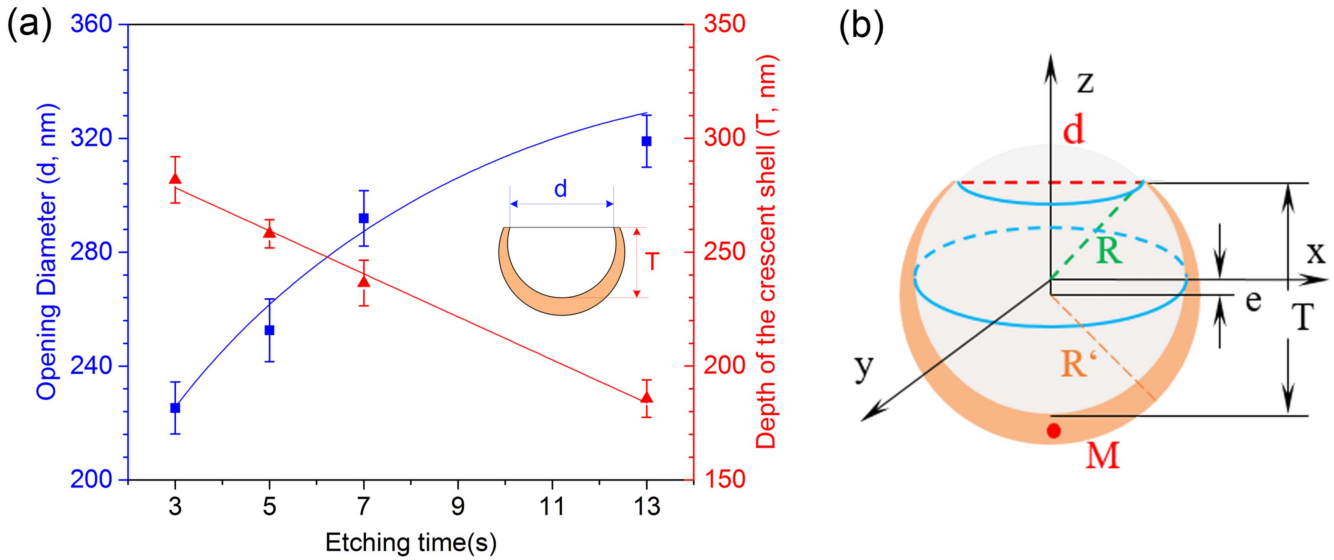

Figure 3. (a) Diagram showing the evolution of the depth T (red triangles) and the hole diameter d (blue squares) of the cavity for increasing etch time. Data points are determined from the SEM and AFM data. Blue and red curves are least square fits for T and d according to the equations (1) and (2), respectively. (b) Schematic of the geometrical parameters used to describe the changes of the a-Si crescent cavity during the etching process, where R and R' are the radii of the inner cavity and the outer shell, and e is the eccentricity of these two spheres.

broken, as the cross sectional image marked by 13′ shows, which suggested that the crescent shell array should not be further etched till the depth T reach the radius of the inner particles. For all the etched samples, the thickness of the a-Si shell at bottom of the cavity are all around 50 nm, which suggests that a-Si crescent shell of the SiO_2/a-Si core/shell particles was gradually etched in the downward direction without damage of lower surface because of the mask of SiO_2 particles array.

In order to quantify the etching process, we extracted the size of the opening diameter d and the depth T of the crescent nanostructures from the SEM and AFM data. The results are plotted as a function of the etching time t as shown in figure 3(a) (d: blue squares, left axis; T: red triangles, right axis; d and T are defined in the inset in figure 3(a) and also in figure 3(b)). It is seen that the diameter of the crescent opening initially increases sharply with the etching time and then slows down to a lower rate. The depth of the crescent shell cavity, measured from the top to the inner bottom of the cavity, decreases with the etching time at a nearly constant rate. A simple model, shown in figure 3(b), was constructed to present the formation of the etched a-Si crescent shells. The model is written in a Cartesian coordinate system whose origin is at the center of the hollow sphere as the origin and the z-axis as the etching direction. In the etching chamber, the reactive ions are accelerated perpendicularly to the sample in a unidirectional electric field. As a result, at the initial etching stage, the top surface of the a-Si shell is preferentially etched, leading to the formation of a hole in the top surface. The size d of the hole increased with etching time t. The depth T of the crescent a-Si shell cavity can be described by equation

$$T(t) = 2R - \upsilon t, \tag{1}$$

where R is the inner (or cavity) radius of the crescent shell and υ is the etching rate in the z direction. Then the depth T decreased linearly with the etching time, which is basically consistent with the measured data. The measured etching rate shows a little slowdown from 7 to 13 s because of a decreased contact area between the reaction species and the a-Si shells. The linear fit of the data of the depth T versus time t allows us to determine the etching rate υ, which is found to be approximately 9.45 nm s^{-1} (see figure 3(a)). The size d of the hole in the normal view can be described by the equation

$$d(t) = 2\sqrt{R^2 - (R - \upsilon t)^2}, \tag{2}$$

which is plotted, for $\upsilon = 9.45$ nm s^{-1}, as smooth curves in figure 3(a). Apparently, the measured depths of the crescent shell array agree reasonably well with the predictions by equation (1). As a result, the etching process for the a-Si crescent shell can be described with a constant etching rate of $\upsilon = 9.45$ nm s^{-1} and the a-Si crescent cavity with different depths T ($R < T < 2R$) can be fabricated by changing the etching time t.

Figure 4(a) shows the simulated and measured transmission spectra of the a-Si crescent shell cavity array. The transmission curves of the a-Si array samples were collected by the UV–vis spectrometer. The FDTD computational simulations were carried out using the commercial software of Lumerical. In the computational model, the structure of a-Si crescent shell was approximately designed by the Boolean subtraction of a silicon sphere of $R' = 185$ nm by a sphere (reflective index $n = 1$) of $R = 160$ nm with off-center distance $e = 25$ nm (see figure 3(b)). Periodic boundary conditions were then applied in the x and y directions to simplify the model for the hexagonal arranged shell array. The x-polarized plane wave with electric intensity E_0 was incident normally on the structure along the negative direction of z. Inspection of figure 4(a) shows that the simulated transmission curves agree well with the experimental data, which suggests that the simulation model is reliable for analyzing the optical property of the nanostructures.

There are two dips (marked by the vertical thin dot dash line) in each curve of the crescent a-Si shell cavity samples with different cavity depths over the discussed wavelength range. For a comparison, the transmission curve of a 50 nm flat a-Si film coated on glass slide also is presented, which is smooth without any valleys due to monotonic transformation of extinction coefficient in the same frequency range. Therefore, the two dips may be caused by the structures of the crescent shell array exciting the WGM at the resonance wavelengths. The transmission dips of the complete spherical shell arrays are understood to be caused by the light at shell size dependent resonance wavelengths confined in the a-Si shell because of the whispering gallery resonance [21, 43]. The reflectance curves of the crescent a-Si shell array with varying depths are plotted in the inset of figure 4(a). The reflectance distinctively changes around the wavelength at which the dips of the transmission curve occur. In order to better understand the light confinement capacity of the crescent shell arrays, the light intensity E at the middle point M of the cavity shell along the negative z direction (see figure 3(b)) was recorded. As figure 4(b) shows, two peaks occur at the wavelengths of $\lambda = \sim680$ nm and $\lambda = \sim570$ nm for these four cases, which agree with the dip wavelengths of the transmission curves. Therefore, it is reasonable to conclude that the confined light at the resonance wavelengths in the crescent shell leads to distinctive dips in the transmission curves. Then the enhanced electric field in the y–z plane of the a-Si crescent shell with an inner diameter of D (or $2R$) $= 320$ nm and depth of $T = 238$ nm at the peak wavelengths are examined. As shown in figures 4(c) and (d), seven and five distinct intensity-enhanced spots occur inside the shell of the a-Si crescent cavity at the peak wavelengths of $\lambda = 553$ nm and $\lambda = 676$ nm, respectively. The seven and five intensity spots inside the crescent a-Si shell are the corresponding WGM [5, 20–22, 24, 43]. Because the a-Si shell was etched with open mouth, the electric intensity enhanced spot on the top was missing at these two electric distribution maps. Then light intensity curves of a point at the same position of a complete crescent shell cavity and spherical shell were added, which were marked with solid triangle. As the figure 4(b) shows, intensity peaks occurred at $\lambda = 701$ nm and $\lambda = 713$ nm respectively, which were due to WGM as the electric distributions at these wavelength (see figures 4(e) and (f)). Compared the intensity enhancement curve of the crescent cavities with the spherical shell, the crescent cavity attains a broadband and a more intensified enhancement of the light intensity near the resonance wavelength. However, for the spherical shell array, a narrow peak with weaker intensity occurred at the resonance wavelength. The incident light can enter easily into the a-Si crescent shell, because the crescent structure array may be collectively viewed as a film of graded average refractive index, and hence more incident of the resonance wavelength occur in stable resonance mode inside the shell.
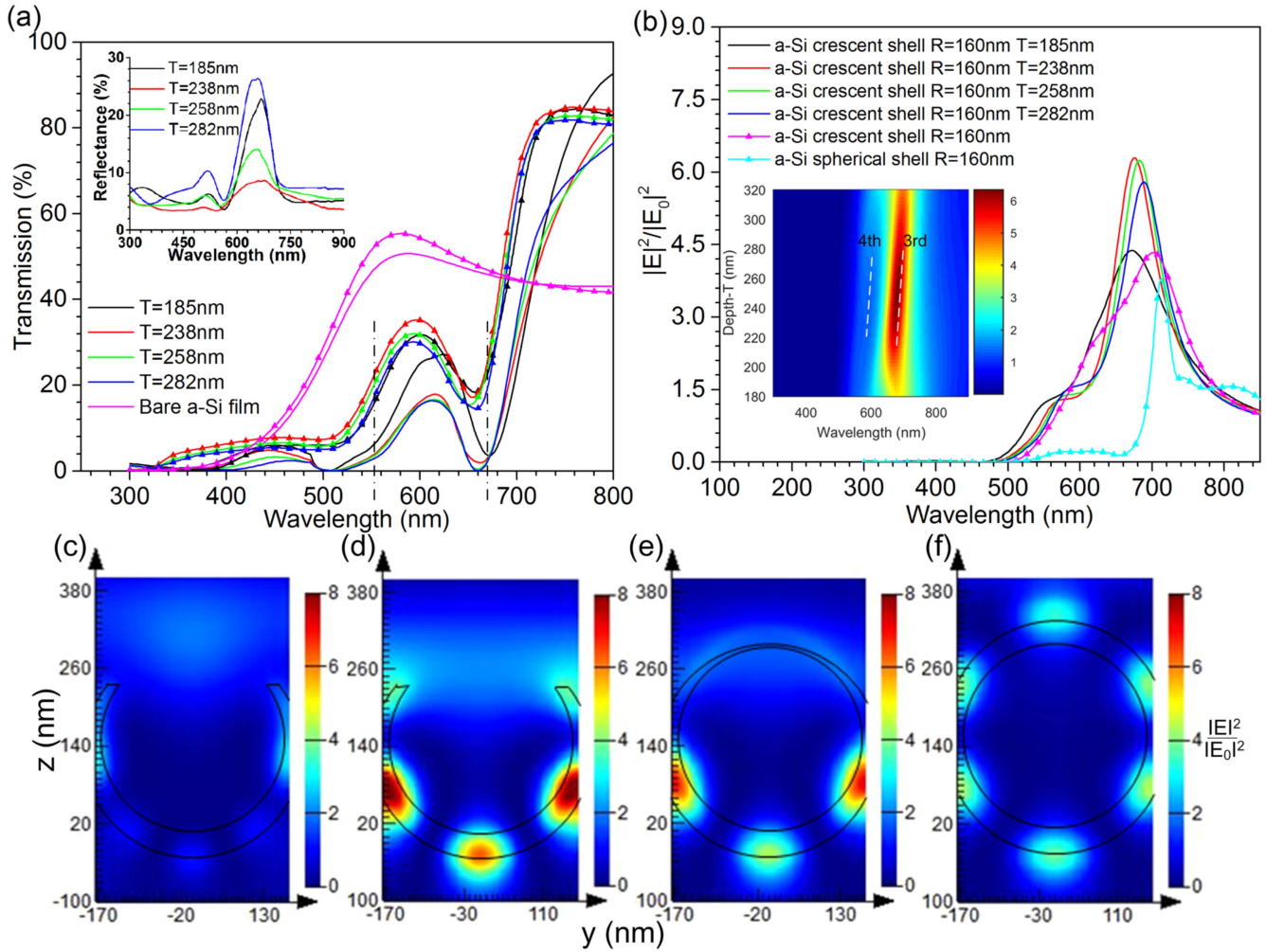
Figure 4. (a) The simulated and measured transmission spectra of the a-Si cavity with different depths, and (b) the light intensity versus wavelength curve for the middle point of the lower layer of the crescent cavity and the complete spherical shell. Inset: contour plot showing light intensity as a function of wavelength and the depth of cavity array. The electric distribution in the *y–z* plane of the cavity with $T = 238$ nm (c), (d), the complete crescent cavity (e) and the $R = 160$ nm complete spherical shell (f) at their resonance wavelength $\lambda = 553$ nm (c), 676 nm (d), 713 nm (e) and 809 nm (f), respectively.

In order to explore the cavity depth related light confinement capacity, light intensity map of point *M* as function of wavelength and cavity depth is plot in the inset of figure 4(b). Two light intensity enhanced areas are clearly presented, which is corresponding to the 3rd and 4th resonances of the whispering galley mode. The resonance positions are blue-shifted with decreased depth of the cavity. The cavity with depth $T = 242.5$ nm obtain the largest light intensity enhancement at the resonance wavelength, which is the trade-off effect of the WGM enhanced intensity and the antireflection. The resonance width of the cavity was diminished with increased depth because of the enhanced light confinement.

The structures of silicon spherical nanoshell have been reported for their enhanced broadband absorption because of the WGM [20]. For the structure of the crescent shell, as discussed above, highlighted enhancement occurred due to the combined effect of WGM and more incident light entering the cavity. The absorption of the cavity shell with depth of $T = 185, 238, 258$ and 282 nm was simulated and measured.

As is evident in figure 5(a), the absorption of the a-Si shell arrays is greatly enhanced when compared with the bare a-Si film and the pristine samples. The simulated curves basically are confirmed by the experimental results, though this is a discrepancy of the peak wavelength shift (see figure 5(b)). For the simulated curves, the peak position is dependent on the depth *T* of the cavity and a decreased *T* makes the peak wavelength blue shifted. For the measured absorption results, the peak wavelength shift is not so distinctive, which may be ascribed to the diffuse reflection at the relatively rough surface of the etched structure.

As shown in figure 5(a), the absorption peaks occur at the resonance wavelength of $\lambda = \sim 670$ nm, which correspond to the dip positions in the transmission curves. The absorption efficiency of the a-Si crescent shell at resonance wavelength increased from $\sim 55\%$ to $\sim 77\%$, with an improvement of $\sim 40\%$, when the shell array was etched with depth of $T = \sim 238$ nm. While for a-Si crescent shell etched with depth of $T = \sim 185$ nm, ~ 258 nm and ~ 282 nm, the absorption efficiency at resonance wavelength increased with an improvement of $\sim 10\%$, $\sim 27\%$
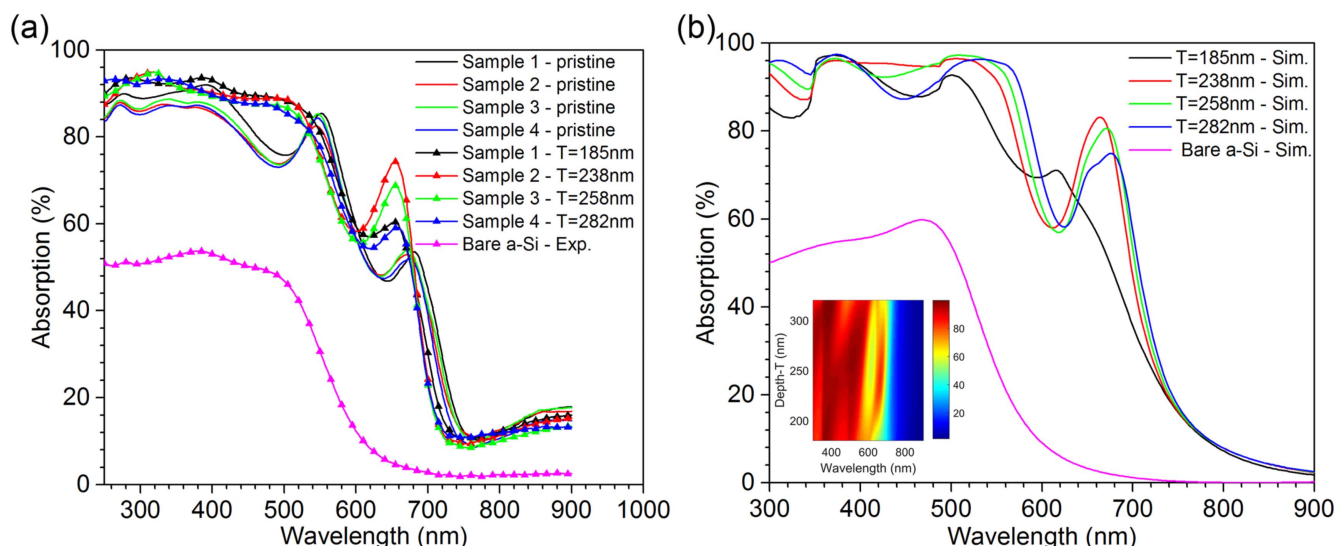
Figure 5. The absorption spectra of a-Si crescent shell arrays with varied depths: (a) measured data, and (b) corresponding FDTD calculations. Inset: contour plot for light absorption efficiency as a function of wavelength and the depth of crescent shell array.

and 9%, respectively. It is worth noting that the crescent shell with $T = \sim 238$ nm has a smaller mass than that with $T = \sim 258$ nm, $T = \sim 282$ nm and the pristine samples. A light absorption efficiency map of the crescent cavity array as a function of wavelength and cavity depth is plotted in the inset of figure 5(b). Clearly, a light absorption enhanced stripe occurs at around $\lambda = \sim 670$ nm and a crescent cavity with $T = 242.5$ nm has the highest light absorption efficiency at the resonance wavelength, which matches well with the light intensity map in figure 4(f). Besides, according to the Mie theory, when SiO_2 particles with larger diameter were used, the resonance wavelength can be redshifted to wavelength near the bandgap of a-Si.

It is important to note that the a-Si crescent shell structures, manufactured as described above, all have shown a significant improvement of light trapping over a broadband wavelength range over the flat surface. Besides, by regulating the depth of the a-Si crescent shell, enhancement around the resonance wavelength is achieved to further improve the absorption efficiency. Indeed, an analysis of the data in figure 5(b) shows an integrated (total) absorption efficiency increase of 10% by varying the cavity depth of the a-Si crescent shell. Though the discussion above is on the cavity depth effect, the inner size can also be important. When the inner cavity size related resonance is also applied, the light trapping capacity of the a-Si crescent shell may be further enhanced.

By employing the fabrication method and the depth-dependent light trapping capacity discussed above, a rational outline of optimal a-Si crescent shell solar cell may be suggested. One possible design would be that the Ag and ITO layers are used as electrodes and the a-Si crescent layer was deposited layer by layer and doped to form n-i-p structure. Since the Ag layer was arranged beneath the a-Si layer, light transmission through the structure could be suppressed and the reflected light could further prolong the effective optical length to enhance light trapping.

Conclusion and outlooks

In conclusion, we have introduced a 2D particle array template assisted PECVD deposition and RIE method for nano-fabricating a periodic crescent a-Si nanoshells. The depth of the crescent cavity can be controlled by the RIE time. Although the current work has described a silicon shell array with an inner size $D = \sim 320$ nm with a resonance wavelength of ~ 670 nm, the structural parameters and the resonance wavelength can be easily regulated by the size of the SiO_2 spheres and appropriate control of etching time. Compared to the complete shell structures, the crescent shell array shows a depth dependent light confinement though enhanced WGM excitation, which can be tuned for a better light absorption efficiency. Among cases studied in this paper, the crescent a-Si cavity array with depth $T = \sim 238$ nm achieves an optimal light absorption and with a smaller volume of a-Si than the cases of $T = \sim 258$ nm and $T = \sim 282$ nm. Therefore, the nanostructure of crescent shell with an optimal depth may be useful in constructing high-efficiency solar cells for light harvesting.

ORCID iDs

Huan Yang ⓘ https://orcid.org/0000-0002-7145-8495
Wei Yu ⓘ https://orcid.org/0000-0002-2113-4046

References

[1] Karg M, König T A F, Retsch M, Stelling C, Reichstein P M, Honold T, Thelakkat M and Fery A 2015 Colloidal self-assembly concepts for light management in photovoltaics *Mater. Today* **18** 185–205

[2] Leung S F, Zhang Q, Tavakoli M M, He J, Mo X and Fan Z 2016 Progress and design concerns of nanostructured solar energy harvesting devices *Small* **12** 2536–48

[3] Yu R, Lin Q, Leung S F and Fan Z 2012 Nanomaterials and nanostructures for efficient light absorption and photovoltaics *Nano Energy* **1** 57–72

[4] Brongersma M L, Cui Y and Fan S 2014 Light management for photovoltaics using high-index nanostructures *Nat. Mater.* **13** 451–60

[5] Grandidier J, Callahan D M, Munday J N and Atwater H A 2011 Light absorption enhancement in thin-film solar cells using whispering gallery modes in dielectric nanospheres *Adv. Mater.* **23** 1272–6

[6] Sang E H and Gang C 2010 Toward the Lambertian limit of light trapping in thin nanostructured silicon solar cells *Nano Lett.* **10** 4692–6

[7] Yu R, Ching K L, Lin Q, Leung S F, Arcrossito D and Fan Z 2011 Strong light absorption of self-organized 3D nanospike arrays for photovoltaic applications *ACS Nano* **5** 9291–8

[8] Garnett E and Yang P 2010 Light trapping in silicon nanowire solar cells *Nano Lett.* **10** 1082–7

[9] Chang H C, Lai K Y, Dai Y A, Wang H H, Lin C A and He J H 2011 Nanowire arrays with controlled structure profiles for maximizing optical collection efficiency *Energy Environ. Sci.* **4** 2863–9

[10] Kelzenberg M D, Boettcher S W, Petykiewicz J A, Turnerevans D B, Putnam M C, Warren E L, Spurgeon J M, Briggs R M, Lewis N S and Atwater H A 2010 Enhanced absorption and carrier collection in Si wire arrays for photovoltaic applications *Nat. Mater.* **9** 239–44

[11] Fan Z, Razavi H, Do J W, Moriwaki A, Ergen O, Chueh Y L, Leu P W, Ho J C, Takahashi T and Reichertz L A 2009 Three dimensional nanopillar array photovoltaics on low cost and flexible substrate *Nat. Mater.* **8** 648–53

[12] Fan Z, Kapadia R, Leu P W, Zhang X, Chueh Y L, Takei K, Yu K, Jamshidi A, Rathore A A and Ruebusch D J 2010 Ordered arrays of dual-diameter nanopillars for maximized optical absorption *Nano Lett.* **10** 3823–7

[13] Wang K X, Fan S, Liu V, Cui Y and Yu Z 2012 Absorption enhancement in ultrathin solar cells with antireflection and light-trapping nanocone gratings *Nano Lett.* **12** 1616–9

[14] Jeong S, Garnett E C, Wang S, Yu Z, Fan S, Brongersma M L, McGehee M D and Cui Y 2012 Hybrid silicon nanocone-polymer solar cells *Nano Lett.* **12** 2971–6

[15] Wang B and Leu P W 2012 Enhanced absorption in silicon nanocone arrays for photovoltaics *Nanotechnology* **23** 194003

[16] Leung S F, Yu M, Lin Q, Kwon K, Ching K L, Gu L, Yu K and Fan Z 2012 Efficient photon capturing with ordered three-dimensional nanowell arrays *Nano Lett.* **12** 3682–9

[17] Sang E H and Gang C 2010 Optical absorption enhancement in silicon nanohole arrays for solar photovoltaics *Nano Lett.* **10** 1012–5

[18] Chen T G, Yu P, Chen S W, Chang F Y, Huang B Y, Cheng Y C, Hsiao J C, Li C K and Wu Y R 2014 Characteristics of large-scale nanohole arrays for thin-silicon photovoltaics *Prog. Photovolt.* **22** 452–61

[19] Zhu J, Hsu C M, Yu Z, Fan S and Cui Y 2015 Nanodome solar cells with efficient light management and self-cleaning *Nano Lett.* **10** 1979–84

[20] Yao Y, Yao J, Narasimhan V K, Ruan Z, Xie C, Fan S and Cui Y 2012 Broadband light management using low-Q whispering gallery modes in spherical nanoshells *Nat. Commun.* **3** 664

[21] Yin J, Zang Y, Yue C, He X, Li J, Wu Z and Fang Y 2013 Self-assembled hollow nanosphere arrays used as low Q whispering gallery mode resonators on thin film solar cells for light trapping *Phys. Chem. Chem. Phys.* **15** 16874–82

[22] Anatolii N O 2002 Whispering-gallery waves *Quantum Electron.* **32** 377–400

[23] Bohren C F and Huffman D R 2008 *Absorption and Scattering of Light by Small Particles* (New York: Wiley)

[24] López-García M, Galisteo-López J F, López C and García-Martín A 2012 Light confinement by two-dimensional arrays of dielectric spheres *Phys. Rev.* B **85** 235145

[25] Gates B D, Xu Q, Stewart M, Ryan D, Willson C G and Whitesides G M 2005 New approaches to nanofabrication: molding, printing, and other techniques *Chem. Rev.* **105** 1171–96

[26] Geissler M and Xia Y 2010 Patterning: principles and some new developments *Adv. Mater.* **16** 1249–69

[27] Salaita K, Wang Y and Mirkin C A 2007 Applications of dip-pen nanolithography *Nat. Nanotechnol.* **2** 145

[28] Guo L J 2007 Nanoimprint lithography: methods and material requirements *Adv. Mater.* **19** 495–513

[29] Perl A s, Reinhoudt D N and Huskens J 2010 Microcontact printing: limitations and achievements *Adv. Mater.* **21** 2257–68

[30] Ye X and Qi L 2011 Two-dimensionally patterned nanostructures based on monolayer colloidal crystals: controllable fabrication, assembly, and applications *Nano Today* **6** 608–31

[31] Vogel N, Retsch M, Fustin C A, Del C A and Jonas U 2015 Advances in colloidal assembly: the design of structure and hierarchy in two and three dimensions *Chem. Rev.* **115** 6265–311

[32] Ai B, Möhwald H, Wang D and Zhang G 2017 Advanced colloidal lithography beyond surface patterning *Adv. Mater. Interfaces* **4** 1600271

[33] Duan G, Cai W, Li Y, Li Z, Cao B and Luo Y 2006 Transferable ordered Ni hollow sphere arrays induced by electrodeposition on colloidal monolayer *J. Phys. Chem.* B **110** 7184–8

[34] Xia X H, Tu J P, Zhang J, Xiang J Y, Wang X L and Zhao X B 2010 Cobalt oxide ordered bowl-like array films prepared by electrodeposition through monolayer polystyrene sphere template and electrochromic properties *ACS Appl. Mater. Interfaces* **2** 186–92

[35] Umh H N, Yu S, Yong H K, Su Y L and Yi J 2016 Tuning the structural color of a 2D photonic crystal using a bowl-like nanostructure *ACS Appl. Mater. Interfaces* **8** 15802–8

[36] Ye X, Li Y, Dong J, Xiao J, Ma Y and Qi L 2013 Facile synthesis of ZnS nanobowl arrays and their applications as 2D photonic crystal sensors *J. Mater. Chem.* C **1** 6112–9

[37] Li C, Hong G, Yu H and Qi L 2010 Facile fabrication of honeycomb-patterned thin films of amorphous calcium carbonate and mosaic calcite *Chem. Mater.* **22** 3206–11

[38] Wang X, Lao C, Graugnard E, Summers C J and Wang Z L 2005 Large-size liftable inverted-nanobowl sheets as reusable masks for nanolithography *Nano Lett.* **5** 1784–8

[39] Zhao X, Wen J, Zhang M, Wang D, Wang Y, Chen L, Zhang Y, Yang J and Du Y 2017 Design of hybrid nanostructural arrays to manipulate SERS-active substrates by nanosphere lithography *ACS Appl. Mater. Interfaces* **9** 7710–6

[40] Li X, Zhang Y, Shen Z X and Fan H J 2012 Highly ordered arrays of particle-in-bowl plasmonic nanostructures for surface-enhanced Raman scattering *Small* **8** 2548–54

[41] Stöber W, Fink A and Bohn E 1968 Controlled growth of monodisperse silica spheres in the micron size range *J. Colloid Interface Sci.* **26** 62–9

[42] Moon G D, Lee T I, Kim B, Chae G, Kim J, Kim S, Myoung J M and Jeong U 2011 Assembled monolayers of hydrophilic particles on water surfaces *ACS Nano* **5** 8600–12

[43] Yin J, Zang Y, Yue C, He X, Yang H, Wu D-Y, Wu M, Kang J, Wu Z and Li J 2015 Multiple coupling in plasmonic metal/dielectric hollow nanocavity arrays for highly sensitive detection *Nanoscale* **7** 13495–502